Hybrid Organic-Inorganic Halide Derivatives of the 2H Hexagonal Perovskite Structure

Noah P. Holzapfel, Alexander Milder, and Patrick M. Woodward*

Department of Chemistry and Biochemistry, The Ohio State University, 100 W. 18th Avenue, Columbus, Ohio 43210, United States

*Corresponding author. Email address: woodward.55@osu.edu

Abstract

Four quaternary hybrid halide perovskites have been synthesized in hydrohalic acid solutions under hydrothermal conditions. The structures of $(CH_3NH_3)_2AgRhX_6$ and $(CH_3NH_3)_2NaRhX_6$, (X = Cl^-, Br^-) consist of infinite one-dimensional chains of face-sharing metal-halide octahedra. The structure is closely related to the 2H hexagonal perovskite structure, but the space group symmetry is lowered from hexagonal $P6_3/mmc$ to trigonal $P\bar{3}m1$ by site ordering of the Rh^{3+} and Ag^+/Na^+ cations. All compositions demonstrate broad-spectrum visible light absorption with optical transitions arising from rhodium *d*-to-*d* transitions and halide-to-rhodium charge transfer transitions. The bromides show a 0.2 eV red shift in the optical transitions compared to the analogous chlorides. Crystal field splitting energies were found to be 2.6 eV and 2.4 eV for the chloride and bromide compositions, respectively. Band structure calculations for all compositions give rather flat valence and conduction bands, suggesting a zero-dimensional electronic structure. The valence bands are made up of crystal orbitals that are almost exclusively Rh 4*d*–Cl 3*p* (Br 4*p*) π^* in character, while the conduction bands have Rh 4*d*–Cl 3*p* (Br 4*p*) σ^* character.

Introduction

Perovskite-based photovoltaics have garnered significant interest due to their efficiencies, which rival that of existing silicon-based technologies.[1] While much of the work has focused on Pb-based materials such as $APbI_{3-x}Br_x$ ($A = CH_3NH_3^+$, $CH(NH_2)_2^+$, Cs^+), concerns about the toxicity of Pb^{2+} persist. One approach to move toward more environmentally friendly compositions is to replace two Pb^{2+} ions with an ordered arrangement of M^+/M^{3+} cations, leading to compounds referred to as double perovskites. Computations have been used to identify double perovskite compositions that have optical properties similar to the Pb^{2+} analogs.[2] This work suggests that $A_2(In^+/Tl^+)(Sb^{3+}/Bi^{3+})X_6$ compositions would possess direct band gaps and exhibit strong optical absorption characteristics. While these compounds may have attractive properties, they do have significant limitations. The toxicity of Tl^+, and to a lesser extent Sb^{3+}, would not be an improvement over the current Pb^{2+} compositions, and the oxidative instability of In^+ is a significant challenge. The most studied halide double perovskites for photovoltaic applications are the $A_2AgBiBr_6$ ($A = Cs^+$ and $CH_3NH_3^+$) compositions, but the indirect and relatively large band gaps of these materials motivates further examination of the double perovskite compositional space.[3,4]

Vishnoi, et al. have recently reported a series of site ordered hexagonal perovskites, $(CH_3NH_3)_2MRuX_6$ ($M = Na^+$, Ag^+, K^+; $X = Cl^-$, Br^-), containing the Ru^{3+} ion.[5] This work expands the hybrid halide double perovskite family to include transition metals other than the d^{10} metals from group 11 (Cu, Ag, Au). While the paramagnetic ground state of Ru^{3+} may not be ideal for photovoltaic applications, the neighboring diamagnetic ion, Rh^{3+} (low-spin d^6), is a potential alternative. $LaRhO_3$ has been shown to behave as a semiconductor rather than a metal or Mott-Insulator, due to the crystal field splitting energy of the 4*d* orbitals.[6] While the high cost of rhodium makes it an unlikely candidate for widespread applications in photovoltaics, it can serve as a good proxy for other low-spin d^6 ions that are more earth abundant, like Co^{3+}. Recent density functional theory (DFT) calculations by Varadwaj and Marques have evaluated the structural stability and optical properties of the cubic double perovskites $A_2AgRhCl_6$ ($A = Li^+$, Na^+, K^+, Rb^+, and Cs^+). Their results predict direct band gap transitions with band gap energies ranging from 0.58 eV for $Cs_2AgRhCl_6$ to 0.66 eV for $Li_2AgRhCl_6$. Band structure and density of states (DOS) calculations suggest the valence band maximum and conduction band minimum arise from a mixture of Rh 4*d* and Cl 3*p* orbitals.[7] Of these compositions, $Cs_2AgRhCl_6$ is the only one that is calculated to be

thermodynamically stable. A similar study on the analogous bromide compositions yielded similar conclusions, with $Cs_2AgRhBr_6$ predicted to be stable.[8]

Here, we report the synthesis and characterization of four quaternary halides containing the Rh^{3+} ion, $(CH_3NH_3)_2MRhX_6$ ($M = Na^+$, Ag^+; $X = Cl^-$, Br^-). Although there is a previous study on the optical properties of Cs_2NaMCl_6 ($M = Y^{3+}$, In^{3+}, Sc^{3+}) doped with Rh^{3+},[9] we are not aware of prior reports of halide perovskites that incorporate Rh^{3+} in stoichiometric quantities. The optical properties of these compounds are indicative of localized transitions associated with isolated $[RhX_6]^{3-}$ octahedra. Band structure calculations show the bands near the Fermi level have minimal dispersion and strongly suggest that these compounds should be thought of as having a zero-dimensional electronic structure. Finally, the structural driving forces that control the competition between cubic and hexagonal perovskite structures are considered.

Experimental

NaCl (GFS Chemicals, 99%), NaBr (Sigma, >99.5%), AgBr (Alfa Aesar, 99.5%) and $RhCl_3 \cdot 3H_2O$ (Matthey Bishop, Lot #33313) were used as received. AgCl was synthesized on a gram scale via precipitation reaction between KCl (Fisher Scientific, 99.8%) and $AgNO_3$ (Alfa Aesar, 99.9%). The resulting white product was washed three times with deionized H_2O and dried overnight via vacuum filtration. While drying, the filter flask was covered with foil to prevent photoreduction of Ag(I) into Ag(0). CH_3NH_3Cl and CH_3NH_3Br were synthesized by the neutralization of methylamine (40 wt. % in H_2O, Sigma-Aldrich) with either HCl (Fisher Scientific, 37%) or HBr (Sigma-Aldrich, 48%) in cold (~ 0 °C) ethanol (Deacon Labs, 200 proof). After neutralization, the solutions were heated to 80 °C and evaporated to dryness. The resulting white powders were ground and transferred to a glass vial, which was placed under vacuum overnight. Typical yields were > 90%. After preparation, the salts were stored in a desiccator.

$(CH_3NH_3)_2AgRhCl_6$ and $(CH_3NH_3)_2NaRhCl_6$ were prepared by adding 4 mmol of CH_3NH_3Cl, 2 mmol of AgCl or NaCl, and 2 mmol of $RhCl_3 \cdot 3H_2O$ to a 23 mL Teflon liner. Next, 5 mL of HCl was added to the liners and the solutions were magnetically stirred for 30 minutes. The liners were then sealed in stainless-steel autoclaves and placed in a box furnace. The autoclaves were heated to 130 °C for 10 hours and then allowed to cool to room temperature at a rate of 5 °C per hour.

The pink/red polycrystalline products were collected via vacuum filtration and washed with diethyl ether (Fisher Scientific, 99.9%). It was found that higher purity samples of $(CH_3NH_3)_2NaRhCl_6$ were obtained when the hydrochloric acid was diluted by mixing 2 mL of HCl and 5 mL of deionized H_2O. $(CH_3NH_3)_2AgRhBr_6$ and $(CH_3NH_3)_2NaRhBr_6$ were prepared in a similar fashion by adding 4 mmol of CH_3NH_3Br, 2 mmol of AgBr or NaBr, and 2 mmol of $RhCl_3 \cdot 3H_2O$ to the Teflon liners. Next, 5 mL of HBr was added to the liners and the solutions were magnetically stirred for 30 minutes. The liners were then sealed in stainless-steel autoclaves and heated in a box furnace following the same scheme as the chlorides. The dark red polycrystalline products were collected via vacuum filtration and washed with diethyl ether. Single crystals were grown using a similar reaction method with the following modification. The amounts of the reactants were reduced by half, the volume of hydrohalic acid was fixed at 5 mL, and the cooling rate was slowed to 3 °C per hour. The violet single crystals were stored in the mother liquor until they were analyzed.

Powder X-ray diffraction (PXRD) data were collected on a Bruker D8 Advance powder diffractometer (40 kV, 40 mA, sealed Cu X-ray tube) equipped with a Lynxeye XE-T position-sensitive detector. The data were collected with an incident beam monochromator (Johansson type SiO_2 crystal) that selects only Cu $K\alpha_1$ radiation (λ = 1.5406 Å). software package to determine the crystal structure.[10] Crystal structure images were generated in Vesta 3.[11]

Single-crystal XRD (SCXRD) studies were carried out on a Bruker D8 Venture diffractometer equipped with a Bruker PHOTON II detector and Mo Kα radiation (λ = 0.7107 Å). Violet plate-like crystals were mounted on MiTeGen MicroMounts with clear enamel. Data were collected at 273 K using φ and ω scans. The crystal-to-detector distance was 50 mm, and the exposure time was 2 s per frame using a scan width of 1.0°. The data were integrated using the Bruker SAINT software program and scaled using the SADABS software program. Solution by intrinsic phasing (SHELXT) produced a complete phasing model for refinement. All atoms were refined with anisotropic displacement parameters via full-matrix least squares (SHELXL-2014).

Differential Scanning Calorimetry (DSC) was performed on a TA Instruments DSC 250 in Tzero aluminum pans. Samples were cooled from 348 K to 183 K under a nitrogen stream of 50 mL/minute with heating and cooling rates of 7 °C/min.

UV-visible diffuse reflectance spectra (DRS) were collected from 250 nm to 800 nm with a PerkinElmer Lambda 950 spectrometer equipped with a 60 mm InGaAs integration sphere. The spectrometer was calibrated using a Labsphere Certified Reflectance Standard. For measurements, approximately 30 mg of sample was diluted in 200 mg of $BaSO_4$ (Sigma-Aldrich, 99.99%).

Density functional theory (DFT) was used to calculate the electronic band structure and density of states (DOS) as implemented with the Quantum ESPRESSO (version 6.1) freeware in combination with the BURAI (version 1.3.1) GUI.[12–14] These calculations were performed using projector augmented wave potentials based on the PBE exchange-correlation functional.[15] Cutoff energies of 407.983 Rydberg and 360.808 Rydberg and a 4 × 4 × 4 k-point grid were used for the Ag- and Na-containing compounds, respectively.[16]

Results

Crystal Structure

The PXRD pattern for $(CH_3NH_3)_2NaRhCl_6$ is shown in Figure 1, the patterns for the other samples can be found in the Supporting Information (Figure S1–S3). $(CH_3NH_3)_2NaRhCl_6$, $(CH_3NH_3)_2AgRhBr_6$, and $(CH_3NH_3)_2NaRhBr_6$ are found to be phase pure. The $(CH_3NH_3)_2AgRhCl_6$ sample contains a small amount of AgCl, but from Rietveld refinement the AgCl content is estimated to be less than 5% by mass. It should be noted that all compositions displayed a significant amount of preferred orientation along the 00*l* crystallographic planes, which limited the accuracy of the structures obtained from analysis of the PXRD data. Consequently, single crystal diffraction methods were used to obtain reliable crystal structures.

It was found that all compositions crystallize in the trigonal space group $P\bar{3}m1$, isostructural with $(CH_3NH_3)_2AgInBr_6$ at room temperature.[17] Although PXRD data could not reliably distinguish between the $P\bar{3}m1$ and $P\bar{3}$ space groups, a $P\bar{3}m1$ structure model resulted in lower R-factors than the $P\bar{3}$ model for all four compounds. A summary of the crystallographic information is given in Table 1, and full details of the refinements can be found in Table S1. Rietveld refinements of the PXRD data using atomic coordinates obtained from SCXRD analysis give good fits, provided a correction for preferred orientation is employed (Figure 1, S1–S3). Bond valence sums (BVS) for the inorganic cations are in good agreement with the expected values, suggesting

stable coordination environments (Table 1). Bond valence parameters for Rh–Cl, Rh–Br, Na–Cl, and Na–Br were taken from Brown, while those for Ag–Cl and Ag–Br were taken from Hull and Berastegui (Appendix A).[18,19]

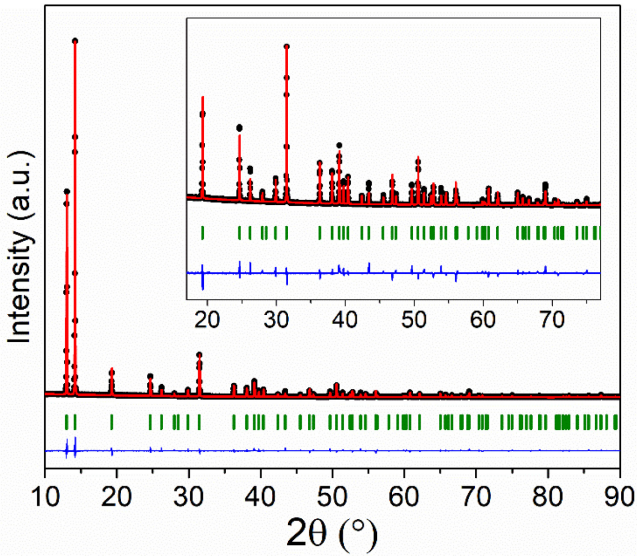

Figure 1: Rietveld refinement of PXRD data for $(CH_3NH_3)_2NaRhCl_6$. Observed data, calculated pattern, difference curves, and main phase are represented by black dots, red curve, blue curve, and green hash marks, respectively.

Table 1: Summary of crystallographic information, metal–halide bond lengths, and bond valence sums (BVS) of the inorganic cations at 273 K (λ = 0.7107 Å) obtained from SCXRD analysis. The $CH_3NH_3^+$ cations are abbreviated as MA.

Composition	**$(MA)_2AgRhCl_6$**	**$(MA)_2NaRhCl_6$**	**$(MA)_2AgRhBr_6$**	**$(MA)_2NaRhBr_6$**
Space Group	$P\bar{3}m1$ (# 164)			
a (Å)	7.1647(8)	7.2184(1)	7.4658(3)	7.4996(1)
c (Å)	6.8150(8)	6.7985(2)	7.0505(6)	7.1075(2)
Volume (Å^3)	302.96(8)	306.78(1)	340.33(4)	346.20(1)
Rh–X distance (Å)	2.3510(6)	2.3506(9)	2.4883(9)	2.4913(3)
Na/Ag–X distance (Å)	2.7894(6)	2.7959(9)	2.8968(9)	2.9357(3)
Rh^{3+} BVS	2.884	2.888	3.216	3.188
M^+ BVS	0.894	1.047	0.903	1.167

The crystal structure of $(CH_3NH_3)_2NaRhCl_6$ is shown in Figure 2. It can be derived from the 2H-hexagonal perovskite structure. The symmetry of all four compounds is lowered from the $P6_3/mmc$ symmetry of the aristotype $BaNiO_3$ structure to $P\bar{3}m1$ by ordering of Rh and Na/Ag. This structure can be described as containing infinite one-dimensional chains of face-sharing octahedra that run parallel to the *c*-axis, with an alternation between Rh^{3+} and Ag^+/Na^+ cations

occupying the octahedral sites. The organic $CH_3NH_3^+$ cations balance the negative charge of the inorganic chains.

Tran et al. observed a phase transition at 135 K for $(CH_3NH_3)_2AgInBr_6$ from the high temperature $P\bar{3}m1$ structure to a low temperature structure with $P\bar{3}$ space group symmetry.[17] This transition is driven by the ordering of the $CH_3NH_3^+$ cations, which leads to displacements of halide ions to optimize hydrogen bonding interactions.[17] Note that $P\bar{3}m1$ and $P\bar{3}$ share the same systematic absences, which makes it difficult to distinguish between the two from laboratory PXRD data. In this study comparisons of fits of the PXRD data using either the $P\bar{3}m1$ or the $P\bar{3}$ structures gave similar fits, but careful analysis of SCXRD data indicated that all four compounds adopt the more symmetric $P\bar{3}m1$ structure at 273 K. In both the $P\bar{3}m1$ and $P\bar{3}$ structures the C–N bond axis lies on the 3-fold axis, but the hydrogen atoms of the $CH_3NH_3^+$ ion can order in $P\bar{3}$, while in $P\bar{3}m1$ their positions are disordered by the mirror planes that intersect the 3-fold rotation axis. This disorder is likely a result of dynamic, rotational motion about the C–N bond axis. DSC data was collected to probe for phase transitions upon cooling (see Figure S4). No transitions were observed over the temperature range measured (348 K to 183 K), suggesting that the $P\bar{3}m1$ to $P\bar{3}$ transition occurs below 183 K in all four compositions studied.

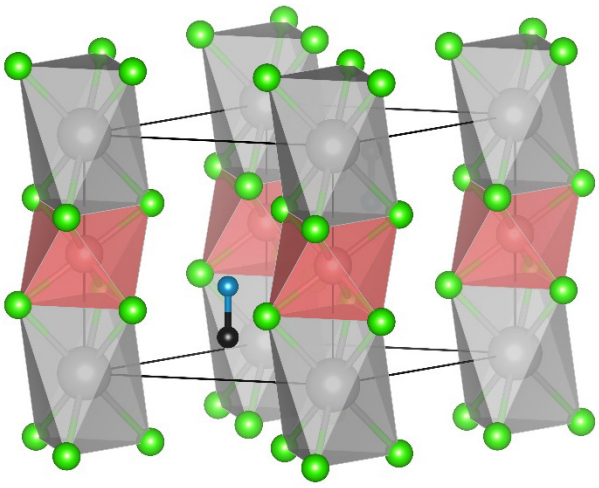

Figure 2: Crystal structure of $(CH_3NH_3)_2NaRhCl_6$. The grey and purple octahedra represent sodium- and rhodium-centered octahedra, respectively. The chloride, carbon, and nitrogen atoms are represented by, green, black, and blue spheres, respectively. The hydrogen atoms are not shown.

Optical Properties

Diffuse reflectance measurements of $(CH_3NH_3)_2AgRhCl_6$ and $(CH_3NH_3)_2NaRhCl_6$ show three distinct absorption bands (Figure 3). The two transitions that lie either fully or partially in the visible region can be assigned to spin-allowed Rh^{3+} *d*-to-*d* transitions. For both compounds the $^1A_{1g} \rightarrow {}^1T_{1g}$ transition appears at 510 nm and the $^1A_{1g} \rightarrow {}^1T_{2g}$ transition at ~415 nm. These values are slightly higher in energy than the absorption maxima of 530 nm and 425 nm found for $Cs_2NaMCl_6:Rh^{3+}$ ($M = Y^{3+}$, In^{3+}, Sc^{3+}). This shift may be attributed to deviations in the Rh–Cl bond length arising from doping Rh^{3+} onto a larger M^{3+} site in the host structure.[9] From the energies of these two transitions and the Tunabe-Sugano diagram for a low-spin d^6 complex, we estimate a crystal field splitting of $\Delta_o = 2.6$ eV (2.1×10^4 cm^{-1}) between the t_{2g} and e_g orbitals, and a Racah parameter B = 0.036 eV (290 cm^{-1}). These values are in good agreement with the values found for a 5.5×10^{-3} M solution of $[RhCl_6]^{3-}$ in 6 M HCl ($\Delta_o = 2.5$ eV and = 0.041 eV).[20] At shorter wavelengths, a rise in absorption occurs that we attribute to a ligand to metal charge transfer (LMCT) transition. The absorbance onset for the LMCT transition in $(CH_3NH_3)_2NaRhCl_6$ begins around 350 nm (3.5 eV) reaching a maximum at 256 nm (4.8 eV), which also agrees with previous spectroscopic studies of $[RhCl_6]^{3-}$ (absorbance onset beginning at 344 nm).[20] The absorption of $(CH_3NH_3)_2AgRhCl_6$ in the UV region of the spectrum is consistently higher than the Na-analog, which may indicate the presence of rhodium to silver metal-to-metal charge transfer (MMCT) transitions.

DRS measurements of the bromide compositions also show prominent features arising from Rh^{3+} *d*-to-*d* transitions (Figure 3). The absorption peak at 550 nm can be attributed to the $^1A_{1g} \rightarrow {}^1T_{1g}$ transition and is seen in both $(CH_3NH_3)_2NaRhBr_6$ and $(CH_3NH_3)_2AgRhBr_6$. The Na-composition also shows a second transition around 450 nm which can be assigned to the $^1A_{1g} \rightarrow {}^1T_{2g}$ transition. From the energies of the two transitions in $(CH_3NH_3)_2NaRhBr_6$, we estimate a crystal field splitting, $\Delta_o = 2.4$ eV (1.9×10^4 cm^{-1}) between the t_{2g} and e_g orbitals, and Racah parameter of B = 0.033 eV (266 cm^{-1}). The LMCT transition in both compounds is red-shifted by ~100 nm with respect to the chloride compositions, well into the visible. This shift is undoubtedly driven by the lower electronegativity of the bromide ion. Here also we see enhanced absorption in the Ag-containing compound, presumably due to Rh to Ag MMCT transitions.

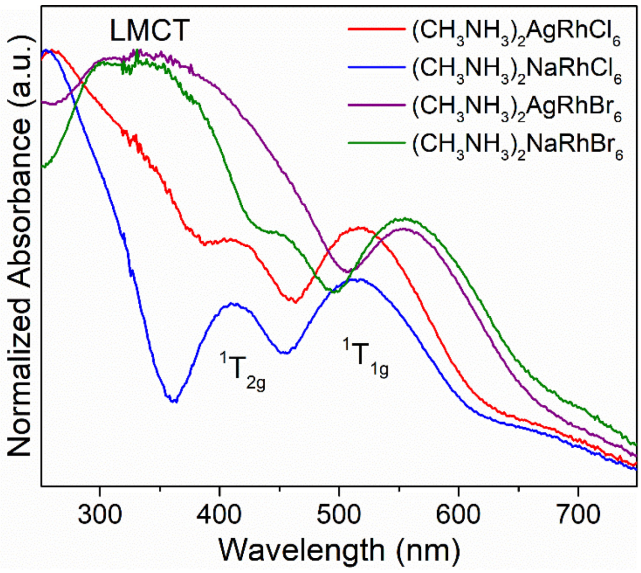

Figure 3: Diffuse reflectance spectra of $(CH_3NH_3)_2AgRhCl_6$ (red), $(CH_3NH_3)_2NaRhCl_6$ (blue), $(CH_3NH_3)_2AgRhBr_6$ (purple), and $(CH_3NH_3)_2NaRhBr_6$ (green). The Rh^{3+} *d*-to-*d* transitions and the LMCT are labeled.

Electronic Band Structure Calculations

Band structure calculations were performed using the structures obtained from the single crystal refinements without geometric relaxation. To simplify the calculations, the $CH_3NH_3^+$ cations were replaced with Cs^+ ions. This simplification is justified as it is generally accepted that Cs^+ and $CH_3NH_3^+$ do not make significant contributions to the band structure near the Fermi level.[4,21] The band structure and density of states (DOS) plots for $(CH_3NH_3)_2NaRhCl_6$ are shown in Figure 4. The calculations show a clear separation into three sets of bands with different orbital parentage: the Cl 3*p* bands (−2.7 to −1.6 eV), Rh t_{2g} bands (−1.0 to −0.6 eV), and Rh e_g bands (+1.1 to +1.5 eV). The latter two sets of bands are most accurately described as having Rh 4*d*–Cl 3*p* π^* and Rh 4*d*–Cl 3*s*/3*p* σ^* character. The partial DOS plots support these assignments. The fact that all bands are quite narrow speaks to the localized nature of the electronic states in this compound. This finding is not terribly surprising given the ionic nature of the bonding between chloride ions and either Na^+ or $CH_3NH_3^+$. This explains why the optical absorption spectrum mirrors that of the $[RhCl_6]^{3-}$ complex anion. The calculations show a direct transition at the M point, although given the relatively flat bands and localized nature of the electronic states it is questionable whether it makes sense to talk about direct and indirect transitions.

The electronic structure does not change much for $(CH_3NH_3)_2AgRhCl_6$, but a new band with Ag 5*s* orbital character emerges that spans the energy range +2.4 eV to +3.3 eV (Figure 4). Since the bands remain relatively narrow we conclude that the valence orbitals on silver do not hybridize extensively with the molecular orbitals of the $[RhCl_6]^{3-}$ anions. The observation that the Ag 5*s* electronic states are higher in energy than the empty Rh 4*d* e_g orbitals is consistent with differences in the diffuse reflectance spectra of the two compounds, which are most pronounced in the near UV. There is also a slight reduction of 0.2 eV in the energy separation of the Rh t_{2g} and Rh e_g bands, but this reduction in the octahedral crystal field splitting is not seen in the optical data where the Rh *d*-to-*d* transitions are at nearly the same energy in both compounds. The energy separation between the Ag 5*s* band and the Rh 4*d* t_{2g} bands on the order of 3–4 eV, which is qualitatively consistent with the assignment of Rh-to-Ag MMCT transitions in the near UV.

Band structure diagrams and DOS plots for the Br-containing samples are given in Figure S5. They are similar to the chlorides but exhibit slightly larger band dispersions in both the valence and conduction bands. It is also seen that Ag 4*d* orbitals make contributions to both the filled π^* bands near the Fermi level and the lower lying Cl 3*p* (Br 4*p*) bands. The introduction of silver leads to a small splitting of the Rh t_{2g} π^* bands, but neither the Ag 4*d* nor the Ag 5*s* orbitals make a meaningful contribution to the Rh e_g σ^* bands. To investigate the potential effects of spin-orbit coupling (SOC), calculations for $(CH_3NH_3)_2AgRhBr_6$ were carried out both with and without SOC (Figure S6). The two results were found to be very similar, so for the sake of simplicity the calculations without spin-orbit coupling are reported here.

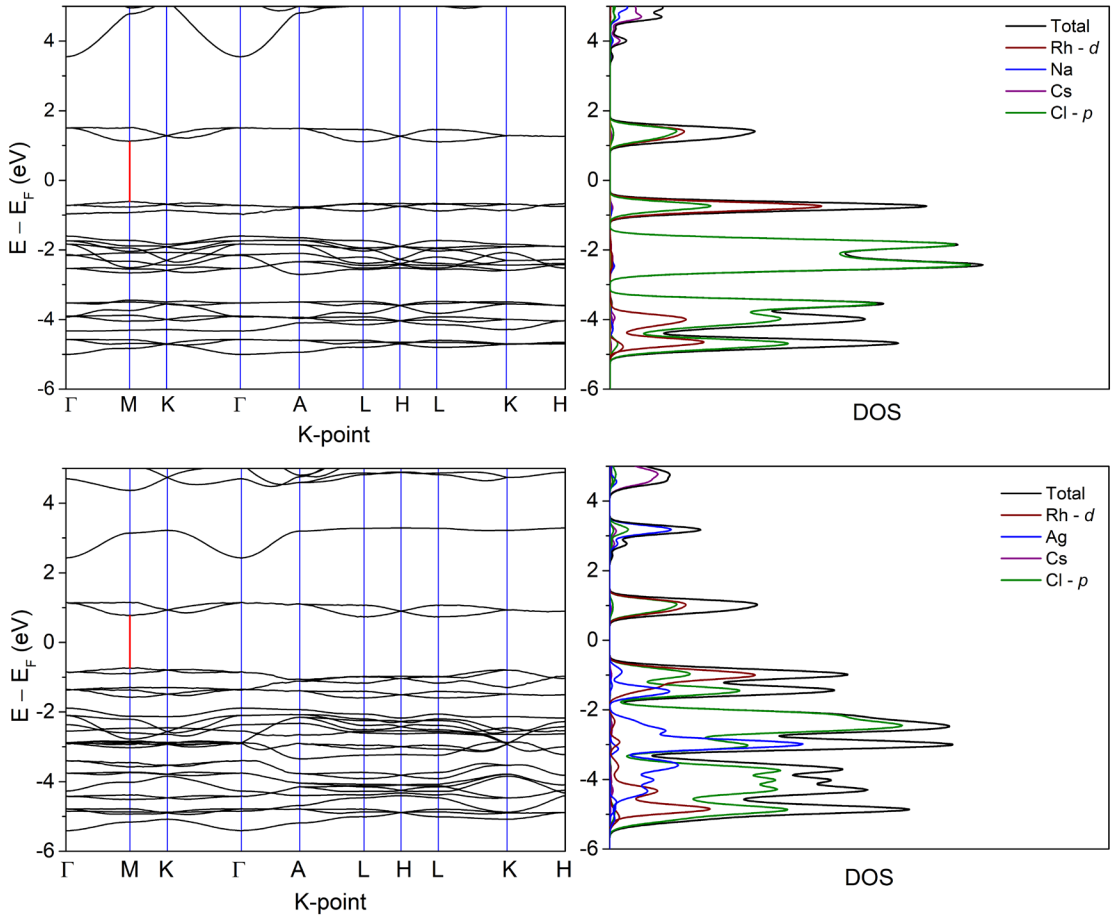

Figure 4: Band structure (left) and total/partial DOS plot (right) for $Cs_2NaRhCl_6$ (top) and $Cs_2AgRhCl_6$ (bottom). Blue lines represent high symmetry k-points, and the red line shows the lowest energy transition from t_{2g} to e_g orbitals of Rh.

Discussion

The optical transitions observed in the DRS as well as the calculated band structures and DOS plots are in good agreement with each other, showing localized transitions originating from the $[RhCl_6]^{3-}$ complex ion. While the presence of infinite face-sharing chains of octahedra might be presumed to lead to a one-dimensional electronic structure, the lack of hybridization between the orbitals of $[RhCl_6]^{3-}$ and those of Ag^+/Na^+ further lowers the dimensionality. It is interesting to compare with the electronic structures of the compounds reported here with that of the cubic double perovskite $Cs_2AgRhCl_6$, as calculated by Varadwaj and Marques. Their calculations show significantly greater dispersion in the Rh e_g σ^* conduction bands, suggesting a greater degree of

hybridization between the two metal sites.[7] Increased band width is generally attractive for photovoltaic applications, and it would be interesting to experimentally compare the properties of a cubic double perovskite like $Cs_2AgRhCl_6$ if this composition can be synthetically realized. This raises an interesting question. What factors control the competition between the cubic perovskite structure and hexagonal variants of the structure?

To understand the relative stability of cubic and hexagonal perovskite structures, one must consider the geometric constraints imposed by the ionic radii. The Goldschmidt tolerance factor, $t = (r_A + r_X)/\left[\sqrt{2}(r_M + r_X)\right]$, describes the relationship between the ionic radii of the A, M, and X sites, denoted by r_A, r_M, and r_X, respectively. For double perovskites, the M-site radius can be estimated as the average of the M^+ and M^{3+} atomic radii.[22] When the tolerance factor is unity, t = 1, a cubic perovskite is expected. However, when $t < 1$, the octahedra may rotate (tilt) to compensate for underbonding of the A-site cation and halide ions. When $t > 1$, a different instability arises. The A–X bonds become too short and both ions become overbonded. To relieve this bond strain, the corner connectivity of the cubic structure can be broken to varying degrees, resulting in a family of structures that are typically referred to as hexagonal perovskites. These structures contain dimers (4H, 6H), trimers (9R), or infinite chains (2H) of face-sharing octahedra.[23] The 2H hexagonal perovskite, which exclusively contains hexagonal packing and face-sharing octahedra, is generally seen for the largest tolerance factors.

Using Equation 1, tolerance factors for a variety of chloride and bromide perovskites were calculated (Table S2) and are plotted in Figure 5. The ionic radii for the M- and X-site cations were taken from the values tabulated by Shannon and the radius for $CH_3NH_3^+$ (2.17 Å) was taken from Kieslich, et al.[24,25] While the use of Shannon radii generally works well for oxides and fluorides, using ionic radii for the heavier halides can lead to inaccurate bond distance estimates. For example, using ionic radii we would predict Rh–Cl distances of 2.475 Å and Rh–Br distances of 2.625 Å, both substantially larger than the experimental distances found in this study of 2.35 Å (Rh–Cl) and 2.49 Å (Rh–Br) (Table 1). It is not straightforward to correct for this effect, because the absolute discrepancies in the bond distance estimates for the larger Cs^+ or $CH_3NH_3^+$ cations are less pronounced than those for the octahedrally coordinated ions. Consequently, the tolerance factors calculated from ionic radii for the heavier halides are lower than what would be obtained

if calculated using parameters that give a more accurate representation of the bond distances.[26] Nevertheless, the tolerance factors calculated from ionic radii can be used to discern relative trends.

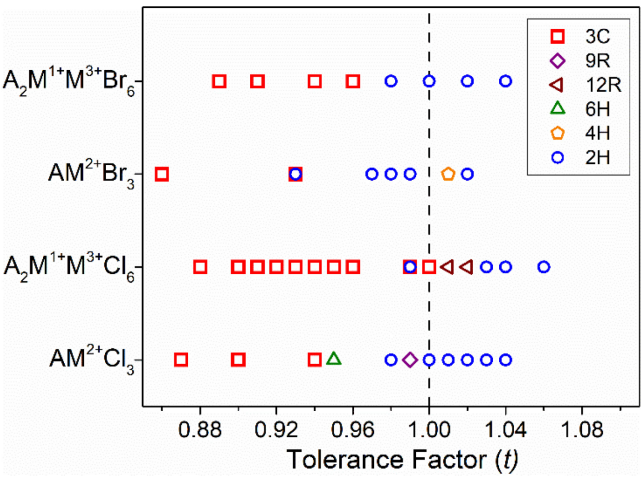

Figure 5: Plot of tolerance factors calculated for different compositions of $AM^{2+}X_3$ and $A_2M^{+}M^{3+}X_6$ perovskites. The vertical dashed line indicates a tolerance factor of unity.

Figure 5 shows that the cubic (3C) structure dominates the lower *t* region (below 0.97), while the 2H structure becomes more favorable for compositions with higher values of *t*. Compositions with a mixture of cubic and hexagonal packing (4H, 6H, 9R, 12R) tend to fall at intermediate values of *t*, although these polytypes are relatively uncommon. Tolerance factors for the four new Rh^{3+} compositions studied here range from 1.02 for $(CH_3NH_3)_2AgRhBr_6$ to 1.06 for $(CH_3NH_3)_2NaRhCl_6$. Because these are the largest values of *t* seen for the $A_2M^{+}M^{3+}Cl_6$ and $A_2M^{+}M^{3+}Br_6$ series, it is not surprising that these compounds adopt a 2H structure.

Figure 5 shows that the cubic structure can be stabilized to higher values of *t* for chlorides than for bromides. We hypothesize that this trend can be traced back to differences in anion polarizability. The ~90° M–X–M bond angles seen in the 2H structure allow for the electron cloud around the halide ion to be polarized toward the inorganic cations, whereas the linear M–X–M bonds of the cubic structure do not permit polarization (in a dipolar sense), because the point symmetry of the halide site (4/*mmm*) possesses an inversion center.[27–29] This effect may also help to explain why the cubic structure is stabilized to higher values of *t* for quaternary double perovskites than it is for ternary perovskites. When the two octahedral cations become different it lowers the site symmetry of the halide site to 4*mm*, which does not have an inversion center.

Consequently, the halide ion can experience a net polarization toward the smaller, more electronegative M^{3+} ion.

Using this survey as a guide, we have calculated the *t* values of $Cs_2AgRhCl_6$, $Cs_2NaRhCl_6$, $Cs_2AgRhBr_6$, and $Cs_2NaRhBr_6$ to be 0.96, 0.98, 0.95, and 0.97, respectively. The tolerance factors for the chloride compositions lie near $Cs_2AgCrCl_6$ ($t = 0.97$) which adopts the 12R structure type, but below Cs_2LiYCl_6 ($t = 0.99$) and $Cs_2LiLuCl_6$ ($t = 1.00$), both of which adopt the cubic structure. $Cs_2NaRhBr_6$ ($t = 0.97$) falls almost exactly where the bromide double perovskites transition from the cubic structure to the 2H structure. Finally, $Cs_2AgRhBr_6$ ($t = 0.95$) has a tolerance factor that is comparable to what is seen in Cs_2NaYBr_6 ($t = 0.94$) and $(CH_3NH_3)_2AgBiBr_6$ ($t = 0.96$), both of which adopt the cubic structure. While this analysis does not conclusively indicate the most stable form of these inorganic Rh-containing double perovskites, it suggests that the cubic structure may be attainable.

Conclusion

Four new hybrid double perovskites containing Rh^{3+} have been synthesized through hydrothermal reaction methods. The crystal structures have been solved through refinement of the SCXRD data and are found to be cation ordered variants of the 2H hexagonal perovskite structure. All four compounds absorb light across much of the visible spectrum through Rh^{3+} *d*-to-*d* transitions, as well as $X^- \rightarrow Rh^{3+}$ LMCT transitions that are seen at higher energies. The UV-visible absorption spectra are very similar to the spectra of solution phase $[RhX_6]^{3-}$ ions, which strongly suggests a zero-dimensional electronic structure. The band structure calculations are fully consistent with this description of the electronic structure. The structural driving factors governing the adoption of the 3C and 2H perovskite structures have been investigated. The relatively small size of Rh^{3+} and the large effective size of $CH_3NH_3^+$ are responsible for the stabilization of the 2H hexagonal perovskite structure over the cubic perovskite structure. Tolerance factor calculations suggest that replacing $CH_3NH_3^+$ with the smaller Cs^+ might lead to stabilization of the cubic perovskite structure, which should have an electronic structure that is more favorable for photovoltaic applications.

AUTHOR INFORMATION

Supporting Information

The Supporting Information is available free of charge on the ACS Publications website.

Details of diffraction experiments, crystallographic data (PDF)

(Figure S1) Rietveld refinement $(CH_3NH_3)_2AgRhCl_6$. (Figure S2) Rietveld refinement $(CH_3NH_3)_2AgRhBr_6$. (Figure S3) Rietveld refinement $(CH_3NH_3)_2NaRhBr_6$. (Table S1) detailed SCXRD refinement report. (Figure S4) DSC measurements. (Figure S5) Band structure/DOS plots hexagonal bromides. (Figure S6) Band structure of hexagonal $Cs_2AgRhBr_6$ with and without SOC. (Table S2) Tolerance factor and structure for halide perovskites.

ORCID

Noah P. Holzapfel: 0000-0002-4566-4033

Alexander Milder: 0000-0002-3143-1482

Patrick M. Woodward: 0000-0002-3441-2148

Author Contributions

The manuscript was written through contributions of all authors. All authors have given approval to the final version of the manuscript.

Notes

The authors declare no competing financial interest.

ACKNOWLEDGEMENT

Funding for N. P. H., A.M., and P. M. W. was provided by the National Science Foundation under award number DMR-2003793.

REFERENCES:

(1) NREL, Best Research-Cell Efficiency Chart https://www.nrel.gov/pv/cell-efficiency.html (accessed Feb 25, 2022).

(2) Meng, W.; Wang, X.; Xiao, Z.; Wang, J.; Mitzi, D. B.; Yan, Y. Parity-Forbidden Transitions and Their Impact on the Optical Absorption Properties of Lead-Free Metal Halide Perovskites and Double Perovskites. *J. Phys. Chem. Lett.* **2017**, *8*, 2999–3007.

(3) Wei, F.; Deng, Z.; Sun, S.; Zhang, F.; Evans, D. M.; Kieslich, G.; Tominaka, S.; Carpenter, M. A.; Zhang, J.; Bristowe, P. D.; Cheetham, A. K. Synthesis and Properties of a Lead-Free Hybrid Double Perovskite: $(CH_3NH_3)_2AgBiBr_6$. *Chem. Mater.* **2017**, *29*, 1089–1094.

(4) McClure, E. T.; Ball, M. R.; Windl, W.; Woodward, P. M. Cs_2AgBiX_6 (X = Br, Cl): New Visible Light Absorbing, Lead-Free Halide Perovskite Semiconductors. *Chem. Mater.* **2016**, *28*, 1348–1354.

(5) Vishnoi, P.; Zuo, J. L.; Strom, T. A.; Wu, G.; Wilson, S. D.; Seshadri, R.; Cheetham, A. K. Structural Diversity and Magnetic Properties of Hybrid Ruthenium Halide Perovskites and Related Compounds. *Angew. Chem. Int. Ed.* **2020**, *59*, 8974-8981.

(6) Nakamura, M.; Krockenberger, Y.; Fujioka, J.; Kawasaki, M.; Tokura, Y. Perovskite $LaRhO_3$ as a p-Type Active Layer in Oxide Photovoltaics. *Appl. Phys. Lett.* **2015**, *106*, 072103.

(7) Varadwaj, P. R.; Marques, H. M. The $Cs_2AgRhCl_6$ Halide Double Perovskite: A Dynamically Stable Lead-Free Transition-Metal Driven Semiconducting Material for Optoelectronics. *Front. Chem.* **2020**, *8*, 796.

(8) Varadwaj, P. R.; Marques, H. M. Physical and Optoelectronic Features of Lead-Free $A_2AgRhBr_6$ (A = Cs, Rb, K, Na, Li) with Halide Double Perovskite Composition. *J. Mater. Chem. C* **2020**, *8*, 12968–12983.

(9) Weaver, S. C.; Donald, S. Optical Absorption and Luminescence Spectra of Rh^{3+} Doped Cs_2NaMCl_6 (M = Y, In, Sc) Single Crystals. *Inorg. Chem* **1992**, *31*, 2814–2820.

(10) Cohelo, A. TOPAS-Academic. *Powder Diffr.* **2007**, 312–317.

(11) Momma, K.; Izumi, F. VESTA 3 for Three-Dimensional Visualization of Crystal, Volumetric and Morphology Data. *J. Appl. Crystallogr.* **2011**, *44*, 1272–1276.

(12) Giannozzi, P.; Baroni, S.; Bonini, N.; Calandra, M.; Car, R.; Cavazzoni, C.; Ceresoli, D.; Chiarotti, G. L.; Cococcioni, M.; Dabo, I.; Corso, A. D.; Gironcoli, S. De; Fabris, S.; Fratesi, G.; Gebauer, R.; Gerstmann, U.; Gougoussis, C.; Kokalj, A.; Lazzeri, M.; Martin-samos, L.; Marzari, N.; Mauri, F.; Mazzarello, R.; Paolini, S.; Pasquarello, A.; Paulatto, L.; Sbraccia, C.; Smogunov, A.; Umari, P. Q UANTUM ESPRESSO : A Modular and Open-Source Software Project for Quantum Simulations of Materials. *J. Phys. Condens. Matter* **2009**, *3*.

(13) Giannozzi, P.; Andreussi, O.; Brumme, T.; Bunau, O.; Nardelli, M. B.; Calandra, M.; Car, R.; Cavazzoni, C.; Ceresoli, D.; Cococcioni, M.; others. Advanced Capabilities for Materials Modelling with Quantum ESPRESSO. *J. Phys. Condens. Matter* **2017**, *29*, 465901.

(14) Nishihara, S. BURAI 1.3 A GUI of Quantum ESPRESSO. https://nisihara.wixsite.com/burai (accessed Nov 11, 2020).

(15) Perdew, J. P.; Burke, K.; Ernzerhof, M. Generalized Gradient Approximation Made Simple. *Phys. Rev. Lett.* **1996**, *77*, 3865–3868.

(16) Pack, J. D.; Monkhorst, H. J. "Special Points for Brillouin-Zone Integrations"-a Reply. *Phys. Rev. B* **1977**, *16*, 1748–1749.

(17) Tran, T. T.; Quintero, M. A.; Arpino, K. E.; Kelly, Z. A.; Panella, J. R.; Wang, X.; McQueen, T. M. Chemically Controlled Crystal Growth of $(CH_3NH_3)_2AgInBr_6$. *CrystEngComm* **2018**, *20*, 5929–5934.

(18) Brown, I. D. *The Chemical Bond in Inorganic Chemistry: The Bond Valence Model*; Oxford University Press, 2002.

(19) Hull, S.; Berastegui, P. Crystal Structures and Ionic Conductivities of Ternary Derivatives of the Silver and Copper Monohalides — II : Ordered Phases within the $(AgX)_x$–$(MX)_{1-x}$ and $(CuX)_x$–$(MX)_{1-x}$ (M = K , Rb and Cs ; X = Cl , Br and I) Systems. *J. Solid State Chem.* **2004**, *177*, 3156–3173.

(20) Ogilvie, F. B.; Holmes, O. G. Visible and Ultraviolet Absorption Spectra of Rhodium(III) in Fused Alkali Chlorides and Nitrates. *Can. J. Chem.* **1966**, *44*, 447–450.

(21) Giorgi, G.; Fujisawa, J. I.; Segawa, H.; Yamashita, K. Small Photocarrier Effective Masses Featuring Ambipolar Transport in Methylammonium Lead Iodide Perovskite: A Density Functional Analysis. *J. Phys. Chem. Lett.* **2013**, *4*, 4213–4216.

(22) Bartel, C. J.; Sutton, C.; Goldsmith, B. R.; Ouyang, R.; Musgrave, C. B.; Ghiringhelli, L. M.; Scheffler, M. New Tolerance Factor to Predict the Stability of Perovskite Oxides and Halides. *Sci. Adv.* **2019**, *5*, 1–10.

(23) Nguyen, L. T.; Cava, R. J. Hexagonal Perovskites as Quantum Materials. *Chem. Rev.* **2021**, *121*, 2935–2965.

(24) Shannon, R. D. Revised Effective Ionic Radii and Systematic Studies of Interatomic Distances in Halides and Chalcogenides. *Acta Crystallog. A* **1976**, *32*, 751–767.

(25) Kieslich, G.; Sun, S.; Cheetham, A. K. An Extended Tolerance Factor Approach for Organic-Inorganic Perovskites. *Chem. Sci.* **2015**, *6*, 3430–3433.

(26) Linaburg, M. R.; McClure, E. T.; Majher, J. D.; Woodward, P. M. $Cs_{1-x}Rb_xPbCl_3$ and $Cs_{1-x}Rb_xPbBr_3$ Solid Solutions: Understanding Octahedral Tilting in Lead Halide Perovskites. *Chem. Mater.* **2017**, *29*, 3507–3514.

(27) Gray, M. B.; Majher, J. D.; Holzapfel, N. P.; Woodward, P. M. Exploring the Stability of Mixed-Halide Vacancy-Ordered Quadruple Perovskites. *Chem. Mater.* **2021**, *33*, 2165–2172.

(28) Mizoguchi, H.; Woodward, P. M.; Byeon, S. H.; Pariset, J. B. Polymorphism in $NaSbO_3$: Structure and Bonding in Metal Oxides. *J. Am. Chem. Soc.* **2004**, *126*, 3175–3184.

(29) Goodenough, J. B.; Kafalas, J. A. Exploring the $A^+B^{5+}O_3$ Compounds. *J. Solid State Chem.* **1973**, *6*, 493–501.

TOC Graphic: